RSC Advances

PAPER

View Article Online
View Journal | View Issue

Cite this: *RSC Adv.*, 2019, **9**, 11932

Three novel polyoxometalate-based inorganic–organic hybrid materials based on 2,6-bis(1,2,4-triazol-1-yl)pyridine†

Yingying Wu, Xuefei Li, Ying Liu, Ge Xiao, Yijiao Huang, Yamin Li,* Dongbin Dang and Yan Bai*

Received 26th February 2019
Accepted 1st April 2019

DOI: 10.1039/c9ra01451a

rsc.li/rsc-advances

Three novel inorganic–organic hybrid materials $[Co(btp)_2(W_5O_{16})(H_2O)]_n$ (**1**), $[Cd_3(btp)_6(PW_{12}O_{40})_2(H_2O)_6\cdot 6H_2O]_n$ (**2**), and $[Ag_3(btp)_2(PMo_{12}O_{40})\cdot 1.5H_2O]_n$ (**3**) (btp = 2,6-bis(1,2,4-triazol-1-yl)pyridine) have been hydrothermally synthesized and characterized by IR spectroscopy, single-crystal X-ray diffraction, powder X-ray diffraction (PXRD), elemental analysis and thermal gravimetric analysis (TGA). The most striking structure feature of compound **1** is a 3D polycatenation framework, interpenetrated by a 2D 4-connected **sql** topology layer and a 3D 6-connected **rob** topology framework. Compound **2** exhibits a rare meso-helices 3D network with different chiralities crossing coexistence. Compound **3** also holds a 3D framework formed by linking terminal oxygen atoms of $[\alpha\text{-}PMo_{12}O_{40}]^{3-}$ anions and silver ions in a 2D metal–organic layer. Compound **1** displays antiferromagnetic behavior. The luminescence, electrochemical and photocatalytic properties of compounds **1–3** have also been investigated. Compound **3** exhibits significant electrochemical activity for the reduction of H_2O_2 while compounds **1** and **2** show efficient photocatalytic activities for the degradation of Rhodamine B (RhB). Furthermore, the three compounds display luminescence behaviors in the solid state.

Introduction

Currently, the design and synthesis of new inorganic–organic hybrid materials, especially polyoxometalate (POM)-based compounds modified by different transition-metals (TMs) and organic ligands, have attracted considerable attention, owing to not only the structural diversities but also the potential applications, such as heterogeneous catalysis, selective absorption, electrochemistry, magnetic functional materials,[1–4] *etc.*

On the one hand, POMs, as one type of transition-metal oxide anionic cluster, can be regarded as "building blocks" with their terminal or bridging oxides coordinating with metal cations. On the other hand, POMs are very good candidates in the synthesis of various multifunctional inorganic–organic hybrid materials because of the following characteristics: (i) the chemically-tunable clusters with negative charges and chemical modifications; (ii) having remarkable catalytic properties; (iii) their tuned acidic and redox properties. An effective strategy to synthesize POM-based inorganic–organic hybrid materials is the combination of POMs clusters into the framework built up from functional organic moieties and desired transition metals (TMs) through the self-assembly methods. So far, numerous inorganic–organic hybrid materials have been obtained, which reveal multifunctional characteristics such as electrocatalytic and photocatalytic activities.[5,6]

Meanwhile, the choice and design of organic ligands are of great importance for exploring new POM-based inorganic–organic hybrid materials.[7–9] Through literature research, many N-heterocyclic organic ligands containing imidazole groups have been used to synthesize POM-based inorganic–organic hybrid materials, such as 1,4-bis(1-imidazoly)benzene, 2,5-bis(1-imidazoly)pyridine, 2,6-bis(1-imidazoly)pyridine.[10–13] By comparison, triazoles and its derivatives, because of their potential $\mu_{1,2}$-, $\mu_{2,4}$-, and $\mu_{1,2,4}$-bridging fashions, are expected to construct more novel functional frameworks with intriguing structural motifs. Some flexible ligands containing triazoles by the introduction of $-(CH_2)_n-$ or phenyl groups have been focused on so as to construct more complicated and variable structural topologies (such as 2,6-bis(1,2,4-triazol-1-yl)benzene, 2,6-bis(1,2,4-triazol-1-yl)ethane, 2,6-bis(1,2,4-triazol-1-yl)propane).[14–17] However, the ligand containing pyridine and double-triazole (2,6-bis(1,2,4-triazol-1-yl)pyridine (btp)), has been paid less attention[18–20] which has the potential to adopt various coordination modes: (a) bridging two metal centers; (b) chelating a metal ion as a terdentate ligand; (c) functioning in modes A and B simultaneously (Scheme 1).

Herein, btp ligand was firstly used to construct three novel POM-based inorganic–organic hybrid materials, namely,

Key Laboratory of Polyoxometalate Chemistry of Henan Province, School of Chemistry and Chemical Engineering, Henan University, Kaifeng 475004, PR China. E-mail: liyamin@henu.edu.cn

† Electronic supplementary information (ESI) available: IR spectra, PXRD patterns, TG curves; additional electrochemical, luminescence, photocatalytic and magnetic characterizations; crystallographic data, bond distances and angles. CCDC 1895048–1895050. For ESI and crystallographic data in CIF or other electronic format see DOI: 10.1039/c9ra01451a

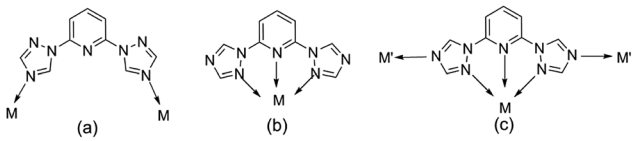

Scheme 1 The potential coordination modes of the ligands.

$[Co(btp)_2(W_5O_{16})(H_2O)]_n$ (**1**), $[Cd_3(btp)_6(PW_{12}O_{40})_2(H_2O)_6\cdot 6H_2O]_n$ (**2**), $[Ag_3(btp)_2(PMo_{12}O_{40})\cdot 1.5H_2O]_n$ (**3**). Different structures are discussed, especially compound **1** displays a rare 3D polycatenation framework interpenetrated by a 2D **sql** layer and a 3D **rob** network while compound **2** bears one unusual meso-helix 3D network constructed left- and right-helices by the metal centers following different axial directions. Furthermore, the electrocatalysis, luminescence properties of compounds **1–3**, photocatalytic properties of compounds **1–3** and the magnetism property of compound **1** are also discussed, respectively.

Experiment section

Materials and methods

All materials were commercially available and used as received without further purification. The FT-IR spectrum was recorded on a Bruker VERTEX-70 FT-IR spectrophotometer in the range of 400–4000 cm^{-1} using KBr pellet. Elemental analysis was carried out on a Vario EL III Etro Elemental Analyzer. Powder X-ray diffraction (PXRD) was gathered on a Bruker D8 Advance diffractometer with CuK_α radiation in the 2θ = 5–50°. Thermogravimetric analysis (TGA) was carried out at room temperature by heating the samples from 25 to 1000 °C under a N_2 ambient air with a heating rate of 20 °C min^{-1} using TGA/DSC3$^+$. Magnetic measurement was carried out on a Quantum Design MPMS-XL SQUID magnetometer.

Synthesis of $[Co(btp)_2(W_5O_{16})(H_2O)]_n$ (1)

A mixture of $CoCl_2\cdot 6H_2O$ (0.3 mmol, 0.071 g), btp (0.2 mmol, 0.042 g), $Na_2H_5P(W_2O_7)_6$ (0.05 mmol, 0.148 g), H_2O (8 mL) was placed in a Teflon-lined stainless steel vessel, stirred until it was uniformly mixed (about 40 minutes), adjust the pH of the solution to about 2.1 with 2 mol L^{-1} HCl during the stirring, and kept at 150 °C for 3 days; then cooled to room temperature over 7–8 h, red block crystals of **1** were obtained and washed with H_2O (yield: 0.033 g, 39.32% based on $Na_2H_5P(W_2O_7)_6$). Anal. calcd (%) for $CoW_5C_{18}H_{16}N_{14}O_{17}$: C, 12.89; H, 0.95; N, 11.70. Found (%): C, 12.88; H, 0.96; N, 11.68. IR (KBr, cm^{-1}): 3426 (w), 1609 (s), 1535 (s), 1468 (s), 1317 (m), 1282 (m), 1222 (m), 1174 (w), 1140 (m), 1107 (w), 977 (*vs.*), 887 (s), 783 (s).

Synthesis of $[Cd_3(btp)_6(PW_{12}O_{40})_2(H_2O)_6\cdot 6H_2O]_n$ (2)

Similar to that of compound **1**, except that $CdCl_2\cdot 2.5H_2O$ (0.3 mmol, 0.069 g) was used as the raw material and the mixture was kept in 180 °C, light yellow block crystals of **2** were obtained and washed with H_2O (yield: 0.078 g, 30.84% based on btp). Anal. calcd (%) for $Cd_3P_2W_{24}C_{54}H_{66}N_{42}O_{92}$: C, 8.56; H, 0.89; N, 7.77. Found (%): C, 8.55; H, 0.88; N, 7.75. IR (KBr, cm^{-1}): 3464 (w), 3130 (w), 1610 (s), 1521 (s), 1476 (m), 1370 (w), 1283 (m), 1218 (m), 1134 (m), 1075 (s), 985 (s), 900 (s), 814 (s).

Synthesis of $[Ag_3(btp)_2(PMo_{12}O_{40})\cdot 1.5H_2O]_n$ (3)

Similar to that of compound **1**, except that $AgNO_3$ (0.1 mmol, 0.017 g) and $H_3PMo_{12}O_{40}$ (0.05 mmol, 0.091 g) were used as the raw materials, golden yellow block crystals of **3** were obtained and washed with H_2O (yield: 0.043 g, 49.63% based on $AgNO_3$). Anal. calcd (%) for $Ag_3PMo_{12}C_{18}H_{17}N_{14}O_{41.5}$: C, 8.33; H, 0.65; N, 7.56. Found (%): C, 8.32; H, 0.66; N, 7.54. IR (KBr, cm^{-1}): 3440 (w), 3120 (w), 1609 (m), 1527 (m), 1460 (m), 1310 (w), 1220 (w), 1171 (w), 1065 (s), 953 (s), 877 (s), 798 (s).

X-ray crystallographic analyses

Single crystal data were collected on Bruker Apex-II CCD area detector diffractometer with graphite-monochromatized MoK_α radiation (λ = 0.71073 Å) at room temperature. Data absorption correction and reduction were made with empirical methods. The structures were solved by direct methods with SHELXS-97 (ref. 21) for compounds **2–3** and SHELXS-2014 (ref. 22) for compound **1**, respectively, and refined by full matrix least-squares methods on F^2 with SHELXL-97 (ref. 23) for compounds **2–3** and SHELXL-2014 (ref. 24) for compound **1**, respectively. Anisotropic displacement parameters were refined for all non-hydrogen atoms. Most hydrogen atoms were localized in their calculated positions and refined using a riding model. Crystal data and refinement for compounds **1–3** are listed in the Table S1 (ESI†) and selected bond length (Å) and bond angles (°) in Table S2–S4 (ESI†). CCDC: 1895048–1895050 for compounds **1–3**, respectively.

Results and discussion

Crystal structure of compound $[Co(btp)_2(W_5O_{16})(H_2O)]_n$ (1)

Single-crystal X-ray analysis reveals that compound **1** crystallizes in orthorhombic space group *Cccm*. Compound **1** exhibits a rare 3D polycatenation framework, which is interpenetrated by a 2D 4-connected **sql** topology layer and a 3D 6-connected **rob** network. As shown in Fig. 1, the asymmetrical unit contains two independent Co(II) atoms, bearing six-coordinate octahedral geometrical configuration. Both of Co(II) atoms are ligated by four nitrogen atoms of btp ligands in the equatorial plane (N1, N1B, N1C and N1D for Co1, N2, N2A, N2E and N2F for Co2, A: $0.5-x, 0.5-y, z$; B: $x, 1-y, 0.5-z$; C: $-x, y, 0.5-z$; D: $-x, 1-y, z$; E: $x, y, -z$, F: $0.5-x, 0.5-y, -z$) with Co–N bond lengths of about 2.066(7) Å, and two oxygen atoms derived from two lattice water molecules (O1W, O1WB for Co1) and the terminal oxygen atoms of two $W_{10}O_{32}^{4-}$ anions (O1, O1A for Co2) in the axial positions with the range of Co–O bond lengths about 2.127(7) −2.320 (10) Å.

As a result, Co1 atoms are bridged by four ligands to form one 2D layered structure in the ab plane, while Co2 atoms coordinated by four ligands and the $W_{10}O_{32}^{4-}$ anion to construct one

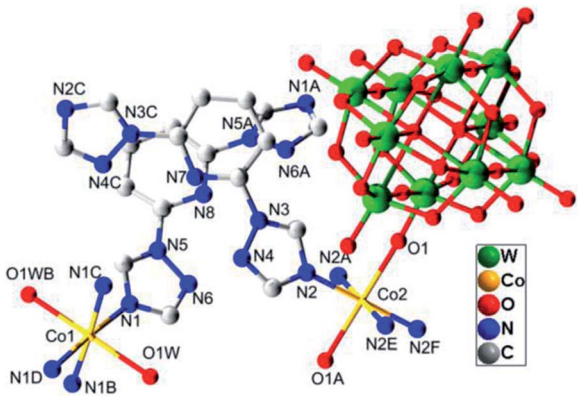

Fig. 1 The coordination diagram of Co(II) atoms in the compound **1**. (Symmetry codes: A: 0.5 − *x*, 0.5 − *y*, *z*; B: *x*, 1 − *y*, 0.5 − *z*; C: −*x*, *y*, 0.5 − *z*; D: −*x*, 1 − *y*, *z*; E: *x*, *y*, −*z*; F: 0.5 − *x*, 0.5 − *y*, −*z*).

3D framework (Fig. 2a and b). From the view point of topology, if the coordinated water molecules are ignored, the 2D layered structure is regarded as a 4-connected **sql** layer with $\{4^4\cdot6^2\}$ topology by simplifying the btp ligands as linear connectors and Co1 ions as a 4-connecting nodes. The 3D network can be rationalized as a 6-connected framework with **rob** topology (point symbol $(4^8\cdot6^6\cdot8)$), in which the Co2 atoms are considered as nodes as well as btp ligands and the $W_{10}O_{32}{}^{4-}$ anions as linkers. It is interesting that the 2D **sql** motifs and the 3D **rob** frameworks are further interpenetrated with each other to form one rare 3D(2D/3D) polycatenation framework (Fig. 2c). Some examples of polycatenation arrays formed by interpenetrating with two motifs are known,[25–29] including 1D + 2D → 2D arrays, 1D + 2D → 3D arrays, 0D + 2D → 2D arrays and 2D + 2D → 3D arrays. However, the polycatenation framework involving 3D and 2D networks is quite unusual.[9,30,31]

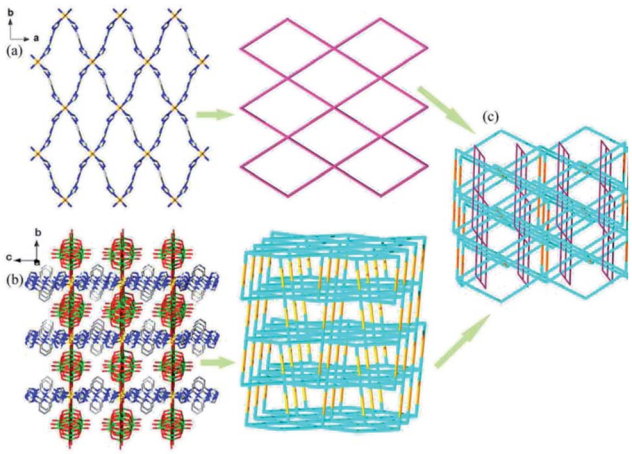

Fig. 2 (a) 2D layered structure and its topological representation in compound **1**. (b) 3D network structure and its topological representation in compound **1**. (c) The topological representation of the 3D(2D/3D) polycatenation framework. Color scheme: W: green; Co: light orange; O: red; N: blue; C: gray. (The hydrogen atoms and the water molecules are omitted for clarity.)

Crystal structure of compound $[Cd_3(btp)_6(PW_{12}O_{40})_2(H_2O)_6\cdot6H_2O]_n$ (2)

Single-crystal X-ray structural analysis shows that compound **2** belongs to cubic $Ia\bar{3}$ space group, forming a rare 3D network structure with different meso-helices crossing coexistence. In compound **2**, the asymmetrical unit contains one independent Cd(II) atom, which bears six-coordinated environment, ligated by four nitrogen atoms (N2, N2D, N7E and N7F, D: 1 − *x*, −1/2 − *y*, *z*; E: 1 + *y*, −3/2 − *z*, −3/2 + *x*; F: −*y*, 1 + *z*, −3/2 + *x*) from four btp ligands and two oxygen atoms from two coordinated water molecules (Fig. 3). The bond length of Cd–N is 2.30(2)–2.35(3) Å, the Cd–O bond length is 2.44(3) Å, and the bond angles of O–Cd–O, N–Cd–N and N–Cd–O are 84(2)° are 94.7(8)–161.1(12)° and 82.1(9)–173.1(11)°, respectively.

Just due to the coordination of Cd–N2 and Cd–N7 (Fig. 4a), the Cd(II) atoms are bridged by the btp ligands to fabricate left- and right-helical chains by 2_1 screw axis with the pitch of 30.375 Å, which are vertical to each other (Fig. 4b) and have the same components transmitted by the alternately linking sequence of N2–Cd–N2 and N7–Cd–N7. As a result, cross-linked meso-helixes 3D network are constructed by the metal ions following different axial directions (Fig. 4c). As far as we know, the meso-helices with different chiralities crossing coexisting in 3D structure are rare,[32,33] which are determined by the high symmetry of compound **2**. Meanwhile, two kinds of cavities are formed with $[\alpha\text{-}PW_{12}O_{40}]^{3-}$ polyoxoanions filled as "guest" cluster anions through electrostatic interactions (Fig. 4d).

Crystal structure of compound $[Ag_3(btp)_2(PMo_{12}O_{40})\cdot1.5H_2O]_n$ (3)

Single-crystal X-ray structural analysis shows that compound **3** belongs to monoclinic $P2_1/n$ space group, which is a 3D framework formed by Ag–O between 2D metal–organic layers and $[\alpha\text{-}PMo_{12}O_{40}]^{3-}$ polyoxoanions. From Fig. 5, the

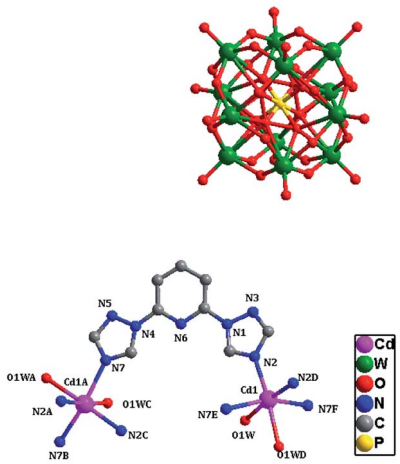

Fig. 3 The coordination diagram of the Cd(II) atoms in compound **2**. (Symmetry codes: A: 3/2 + *z*, −1 + *x*, −3/2 − *y*; B: *x*, −1 − *y*, −5/2 − *z*; C: 3/2 + *z*, −*x*, −1 + *y*; D: 1 − *x*, −1/2 − *y*, *z*; E: 1 + *y*, −3/2 − *z*, −3/2 + *x*; F: −*y*, 1 + *z*, −3/2 + *x*). (The hydrogen atoms and crystal water molecules are omitted for clarity.)

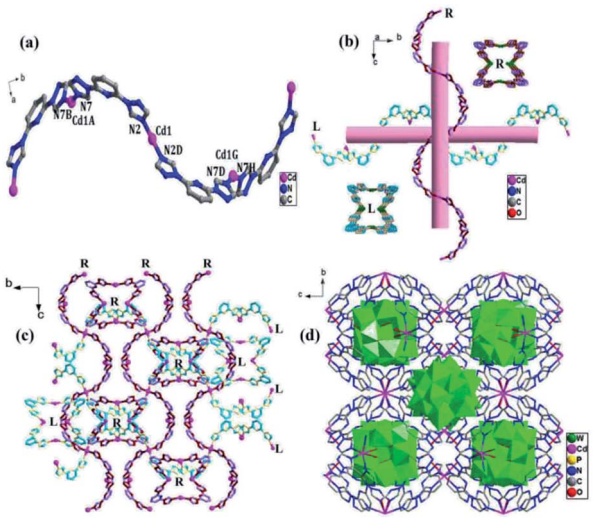

Fig. 4 (a)–(c) The pseudo-helical chains in compound **2**. (Symmetry codes: A: 3/2 + *z*, −1 + *x*, −3/2 − *y*; B: *x*, −1 − *y*, −5/2 − *z*; D: 1 − *x*, −1/2 − *y*, *z*; G: −1/2 − *z*, 1/2 − *x*, −3/2 − *y*; H: 1 − *x*, 1/2 + *y*, −5/2 − *z*). (d) The 3D network of compound **2**. The color scheme for (b) and (c): Cd: pink; N: yellow and dark red; C: sky blue and purple. (The hydrogen atoms and crystal water molecules are omitted for clarity.)

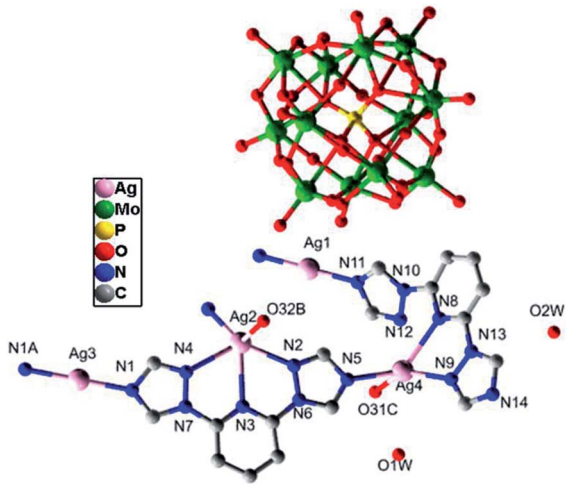

Fig. 5 The coordination diagram of Ag(I) atoms in the compound **3**. (The hydrogen atoms are omitted for clarity.) (Symmetry codes: A: −1 − *x*, 2 − *y*, −1 − *z*; B: −0.5 − *x*, −0.5 + *y*, −0.5 − *z*; C: −*x*, 3 − *y*, −1 − *z*).

asymmetrical unit of compound **3** contains four Ag(I) atoms. Ag1 and Ag3 atoms bear linear geometries formed by two nitrogen atoms from two btp ligands with Ag–N lengths of 2.143(5)–2.161(5) Å and N–Ag–N of about 179.998(1)–180.0°. Ag2 and Ag4 atoms are coordinated to two nitrogen atoms derived from two btp ligands with N–Ag–N of about 62.42(16)° and 67.25(17)° and Ag–N lengths of 2.222(5) to 2.315(5) Å, respectively. Besides, Ag2 is also weak connected to two nitrogen atoms from the same btp ligand and one oxygen atom from one $[\alpha\text{-}PMo_{12}O_{40}]^{3-}$ polyoxoanion, and Ag4 atom forms weak interactions with one nitrogen atom from one btp ligand and one oxygen atom from one $[\alpha\text{-}PMo_{12}O_{40}]^{3-}$ polyoxoanion. The Ag–O and Ag–N bond lengths range from 2.640(43) to 2.696(45) Å and 2.514(9) to 2.564(6) Å, respectively. As a result, Ag2 atom is five coordinated in a pyramid geometry environment while Ag4 atom is in a tetrahedral configuration.

As shown in the Fig. 6a and b, different from those of compounds **1** and **2**, two coordination modes of btp ligands (A: μ_3-η^1:η^1:η^1:η^1; B: μ_3-η^1:η^1:η^1:η^1:η^1) are observed in compound **3**, which link different Ag toms into 2D metal–organic layers (Fig. 6c). The 2D layers are further connected by Ag–O from $[\alpha\text{-}PMo_{12}O_{40}]^{3-}$ anions to generate a 3D framework (Fig. 6d).

IR spectra, thermal stability and XRD

The IR spectra of **1–3** display the characteristic absorption bands of btp ligands. The characteristic peaks of 1609 cm^{-1}, 1535 cm^{-1}, 1468 cm^{-1} for **1**, 1610 cm^{-1}, 1521 cm^{-1}, 1476 cm^{-1} for **2**, 1609 cm^{-1}, 1527 cm^{-1}, 1460 cm^{-1} for **3** can be indicated the existence of btp ligands.[34] The strong peaks at 783 cm^{-1}, 887 cm^{-1} and 977 cm^{-1} for **1** are attributed to the ν (W–O_c), ν (W–O_b) and ν (W–O_d); 814 cm^{-1}, 900 cm^{-1}, 985 cm^{-1} and 1075 cm^{-1} for **2** are assigned to the ν (W–O_c), ν (W–O_b), ν (W–O_d) and ν (P–O_a); 789 cm^{-1}, 877 cm^{-1}, 953 cm^{-1} and 1065 cm^{-1} for **3** can be attributed to the ν (Mo–O_c), ν (Mo–O_b), ν (Mo–O_d) and ν (P–O_a), respectively (Fig. S1, ESI†). All of the above demonstrate the presence of polyacid anions in the compounds **1–3**.

The thermogravimetric analyses of the compounds **1–3** have been investigated under N_2 atmosphere with the heating test range of 25–1000 °C by TGA. As shown in Fig. S2 (ESI†), the experimental results show that compounds **1–3** have high stability and exhibit similar two-step weight loss with the

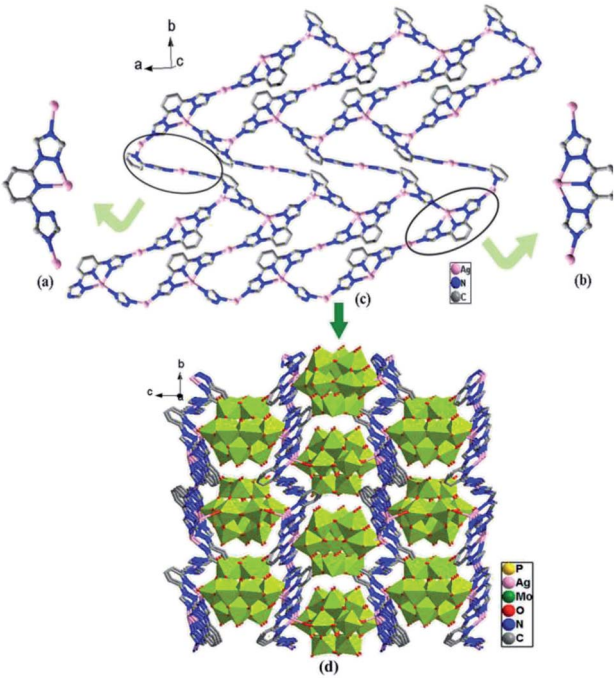

Fig. 6 (a) Coordination mode A of the btp ligand. (b) Coordination mode B of the btp ligand. (c) The 2D sheet. (d) The 3D network structure of the compound **3**. (The hydrogen atoms and crystal water molecules are omitted for clarity.)

temperature for collapse of skeleton of about 391 °C for compound **1**, 299 °C for compound **2** and 334 °C for compound **3**.

In order to check the phase purities of the bulky solid sample for compounds **1–3**, the X-ray powder diffractions of compounds **1–3** were carried out at room temperature with the angle in the range of 5–50°. As shown in Fig. S3 (ESI†), peaks of experimental patterns are in good agreement with as-synthesized diffraction peaks for compounds **1–3**, which confirm the pure phase of the samples. The differences in intensity are because of the preferred orientation of crystalline powder samples.[35]

Electrochemical properties of compounds 1–3

The glassy carbon electrodes (GCEs) become an optimal choice for studying the electrochemical properties of compounds **1–3**, because of their good electrical conductivities and high chemical stabilities.[36–38] In order to investigate the electrochemical behaviors of compounds **1–3**, the three compounds have been used as modifiers to fabricate chemically modified electrodes (**1**–GCE, **2**–GCE and **3**–GCE). The cyclic voltammetric behaviors for **1**–GCE, **2**–GCE and **3**–GCE in 0.5 mol L^{-1} Na_2SO_4 + 0.01 mol L^{-1} H_2SO_4 aqueous solution at different scan rates were recorded with the scan rate varying from 80 to 200 mV s^{-1} for **2**–GCE, from 50 to 200 mV s^{-1} for **1**–GCE and **3**–GCE. In the potential range of −850 to 350 mV for **1**–GCE, there are three pairs of reversible redox peaks (I–I′, II–II′ and III–III′), and the mean peak potentials $E_{1/2} = (E_{pa} + E_{pc})/2$ of approximately −519.90, −294.88 and −114.79 mV can be clearly observed (Fig. 7a), which is attributed to two consecutive one-electron processes and one two-electron process of W atoms.[39] For **2**–GCE, two redox peaks (I–I′, II–II′) appear in the potential range of −100 to 400 mV (Fig. 7b), and the mean peak potentials $E_{1/2} = (E_{pa} + E_{pc})/2$ are −675.63, −232.05 mV, respectively. Moreover the redox peaks I–I′ and III–III′ may be assigned to two consecutive two-electron redox processes of W centers.[40] The **3**–GCE has four reversible redox couples (I–I′, II–II′, III–III′ and IV–IV′) in the scan range of −0.4–0.6 V (Fig. 7c), which is mainly derived from the redox process of $PMo_{12}O_{40}^{3-}$ anions, and the corresponding half-wave potential $E_{1/2} = (E_{pa} + E_{pc})/2$ are located at −342.21, −252.56, 40.52 and 284.73 mV, respectively.[41] At the same time, the peak potentials change gradually following the scan rates 80–200 mV s^{-1} for **2**–GCE, 50–200 mV s^{-1} for **1**–GCE and **3**–GCE (Fig. S4, ESI†): the cathodic peak potentials shift toward the negative direction and the corresponding anodic peak potentials move to the positive direction. The peak currents are proportional to the square root of the scan rates up to 200 mV s^{-1}, which indicates that the redox process of the **1–3**–GCE is surface-controlled.[42] In addition, electrocatalytic reduction for H_2O_2 of **3**–GCE was also investigated. As shown in Fig. 7d, with the addition of H_2O_2, the four reduction peak currents increase markedly while the corresponding oxidation peak currents decrease, suggesting that the **3**–GCE has good electrocatalytic activity for the reduction of H_2O_2.

Photocatalytic properties of compounds 1–3

It is known that a wide range of POMs have photocatalytic activities during the degradation of organic dyes under UV irradiation. Therefore, the photocatalytic properties of POMs have a wide range of potential applications in purifying water quality.[43] Herein, Rhodamine B (RhB) was used to investigate the photocatalytic performance of compounds **1–3** upon UV irradiation from a 300 W Hg lamp. Moreover, the photodegradation process of RhB without catalyst has also been studied under the same conditions (Fig. S5, ESI†). It can be clearly observed that the absorption peaks of RhB containing compounds **1–2** decrease obviously with increasing of reaction time (Fig. 8a and b). The calculations display that the degradation ratio of RhB was 84.44% for compound **1** and 85.14% for compound **2** after about the irradiation of 3.5 hours. Comparatively, the degradation ratio of RhB for compound **3** was 29.90%, which was lower than those of compounds **1** and **2** (Fig. S6, ESI†). The results indicate that compounds **1–2** have

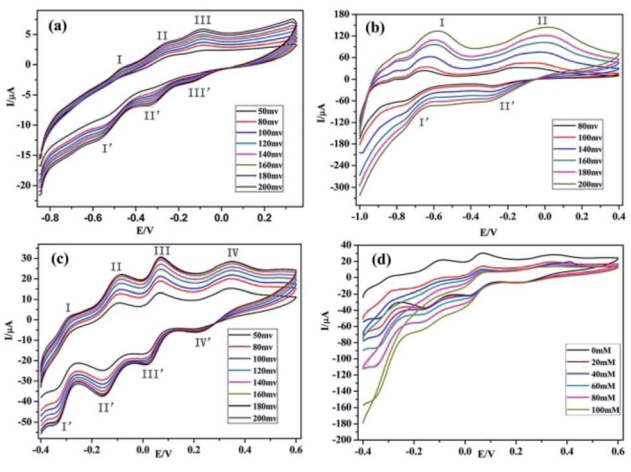

Fig. 7 (a)–(c) The cyclic voltammetric behaviors at different scan rates in 0.5 mol L^{-1} Na_2SO_4 + 0.01 mol L^{-1} H_2SO_4 solution for **1**–GCE, **2**–GCE and **3**–GCE. (d) The electrocatalytic activity to reduce H_2O_2 in 0.5 mol L^{-1} Na_2SO_4 + 0.01 mol L^{-1} H_2SO_4 solution at the scan rate 200 mV s^{-1} for **3**–GCE.

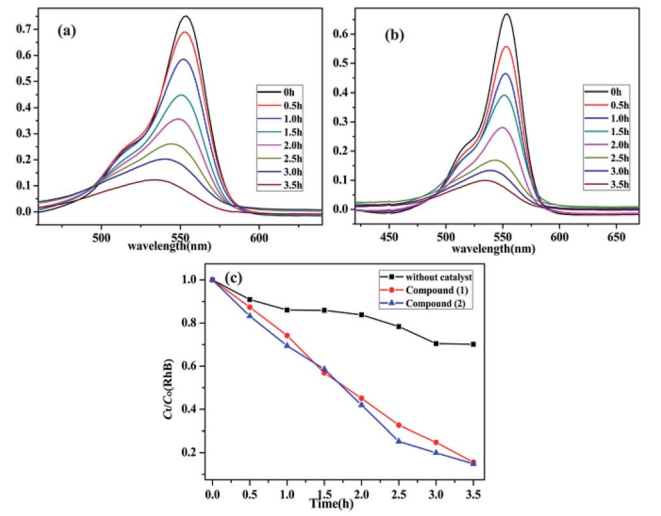

Fig. 8 (a) and (b) Absorption spectra of the RhB (10 mg L^{-1}) solution during the decomposition reaction under UV light irradiation with the use of compound **1** and **2**. (c) The comparison of the two compounds and no crystal decomposition rate of RhB in the same conditions.

good photocatalytic activities for the degradation of RhB, which may be good candidates for photocatalysis to degrade the certain organic dyes (Fig. 8c).

Luminescent properties of compounds 1–3

The solid-state photoluminescence of complexes **1–3** and the btp ligands were carried out at room temperature. As shown in the Fig. S7 (ESI†), the free btp ligands display two intense emissions at 442 and 466 nm upon excitation at 230 nm, while the main emission peaks are observed at about 430 and 454 nm for compound **1**, 434 and 458 nm for compound **2**, 435 and 459 nm for compound **3** upon the excitation of 230 nm, respectively. Compared by those of btp ligand, there is an obvious blue-shift of about 7–12 nm for three compounds. It can be inferred that those peaks originates from the π*–π transition of btp ligands.[44,45] In order to further investigate the photoluminescent properties, luminescent decay curve was carried out by checking the emission at 454 nm (compound **1**), 458 nm (compound **2**) and 459 nm (compound **3**), which can be well fitted into a double-exponential decay function as $I = A_1 \exp(-t/\tau) + A_2 \exp(-t/\tau)$, affording the lifetime: $\tau_1 = 938.66$ ns (78.17%) and $\tau_2 = 8271.71$ ns (21.83%) for compound **1**, $\tau_1 = 1000.00$ ns (58.00%) and $\tau_2 = 8043.97$ ns (42.00%) for compound **2**, $\tau_1 = 1037.39$ ns (64.92%) and $\tau_2 = 8415.63$ ns (35.08%) for compound **3**, the pre-exponential factor: $A_1 = 1853.76$, $A_2 = 58.74$ (compound **1**) (Fig. 9a); $A_1 = 1357.10$, $A_2 = 122.15$ (compound **2**) (Fig. 9b); $A_1 = 1610.91$, $A_2 = 107.32$ (compound **3**) (Fig. 9c). Therefore, the average lifetime of 2.5393 μs for compound **1**, 3.9582 μs for compound **2**, 3.6260 μs for compound **3** based on the formula $\tau = (A_1\tau_1^2 + A_2\tau_2^2)/(A_1\tau_1 + A_2\tau_2)$.[46]

Magnetic property of compound 1

The temperature-dependent magnetic susceptibility data of compound **1** is measured for the crystal samples in the 2–300 K temperature range under an applied field of 1000 Oe. The $\chi_m T$ and χ_m^{-1} *versus* T are shown in the Fig. 10. The $\chi_m T$ value is 3.296 cm^3 mol^{-1} K at 300 K, which is smaller than the expected (3.75 cm^3 mol^{-1} K) for one isolated Co(II) ion ($g = 2.5$, $S = 3/2$).[47] As the

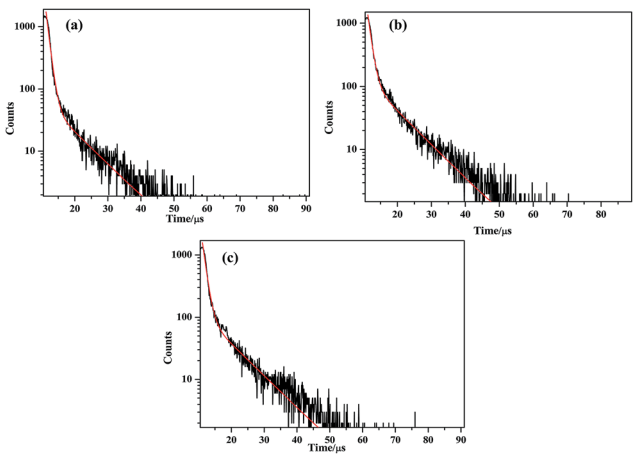

Fig. 9 (a)–(c) The luminescence decay curves taken by monitoring the emission at 454 nm for compounds **1–3**.

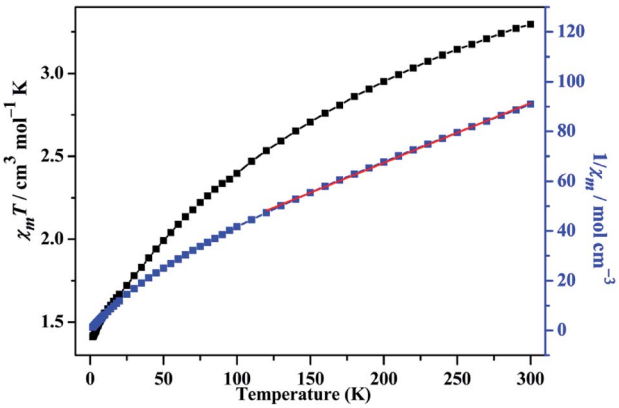

Fig. 10 The $\chi_m T$ *vs.* T and χ_m^{-1} *vs.* T plots of **1** in the range of 2–300 K at 1000 Oe, the red solid line represents the best fit.

temperature decreasing, the $\chi_m T$ value continuously reduces to 1.414 cm^3 mol^{-1} K at 2 K, which is an indicative to the presence of antiferromagnetic exchange interactions between the Co(II) magnetic centers. The temperature dependence of the reciprocal susceptibility χ_m^{-1} of compound **1** obeys the Curie–Weiss law in the temperature range of 120–300 K, giving $C = 4.160$ cm^3 mol^{-1} K, $\theta = -80.374$ K, which further confirm the antiferromagnetic interaction between Co(II) ions. To further investigate the magnetic interactions, the variation of magnetizations with field strengths was also tested at 2 K (Fig. S8, ESI†). The M value is 2.072 Nβ when the field reaches 7 T, lower than the expected value of 3.75 Nβ, which is also characteristic of antiferromagnetic interaction.

Conclusion

In conclusion, three novel inorganic–organic hybrid materials $[Co_2(btp)_4(W_{10}O_{32})(H_2O)_2]_n$ (**1**), $[Cd_3(btp)(PW_{12}O_{40})_2(H_2O)_6 \cdot 6H_2O]_n$ (**2**), $[Ag_3(btp)_2(PMo_{12}O_{40}) \cdot 1.5H_2O]_n$ (**3**) (btp = 2,6-bis(1,2,4-triazol-1-yl)pyridine) have successfully been synthesized through hydrothermal methods. Three compounds exhibit 3D frameworks of various structures due to different coordination modes of the ligands, different coordination environment of the metal ions and different polyoxoanions. Compound **1** is a rare 3D polycatenation framework, interpenetrated by a 2D 4-connected **sql** layer with $\{4^4 \cdot 6^2\}$ topology and a 3D 6-connected framework with **rob** network structure with $\{4^8 \cdot 6^6 \cdot 8\}$ topology; the unusual meso-helices 3D network of compound **2** comprises of the crossing left- and right-helical chains following different axial directions while the 3D framework is formed by 2D metal–organic layer connected by Ag–O bond from $[\alpha\text{-}PMo_{12}O_{40}]^{3-}$ anions in compound **3**. In addition, the magnetism of compound **1**, the luminescent, photocatalytic and electrochemical properties of compounds **1–3** have been investigated. The results show that three compounds display luminescent behaviors at solid state. In addition, compound **1** displays antiferromagnetic behavior, compounds **1–2** show efficient catalytic activities for the degradation of Rhodamine B (RhB), and compound **3** exhibits significant electrochemical activity for the reduction of H_2O_2.

Conflicts of interest

There are no conflicts to declare.

Acknowledgements

The research is financially supported by the National Natural Science Foundation of China (U1504209, 21403053), Young Backbone Teacher Project of Henan Colleges and Universities (2016GGJS-023) and Foundation of Henan University (0000A40478).

Notes and references

1 W. Salomon, E. Rivière, X. López, N. Suaud, P. Mialane, M. Haouas, A. Saad, J. Marrot and A. Dolbecq, *Dalton Trans.*, 2018, **47**, 10636–10645.
2 M. S. S. Balula, I. C. M. S. Santos, J. A. F. Gamelas, A. M. V. Cavaleiro, N. Binsted and W. Schlindwein, *Eur. J. Inorg. Chem.*, 2007, **7**, 1027–1038.
3 C. G. Liu, S. Liu and T. Zheng, *Inorg. Chem.*, 2015, **54**, 7929–7935.
4 M. Carraro and S. Gross, *Materials*, 2014, **7**, 3956–3989.
5 X. F. Li, X. Wang, Y. Y. Wu, X. W. Zhao, H. Y. Li and Y. M. Li, *J. Solid State Chem.*, 2019, **269**, 118–124.
6 X. F. Li, Y. Y. Wu, H. J. Lun, H. Y. Li, J. H. Yang and Y. M. Li, *Synth. Met.*, 2017, **232**, 103–110.
7 X. J. Yang, M. Sun, H. Y. Zang, Y. Y. Ma, X. J. Feng, H. Q. Tan, Y. H. Wang and Y. G. Li, *Chem.–Asian J.*, 2016, **11**, 858–867.
8 S. B. Li, L. Zhang, K. P. O'Halloran, H. Y. Ma and H. J. Pang, *Dalton Trans.*, 2015, **44**, 2062–2065.
9 X. L. Hao, Y. Y. Ma, Y. H. Wang, L. Y. Xu, F. C. Liu, M. M. Zhang and Y. G. Li, *Chem.–Asian J.*, 2014, **9**, 819–829.
10 W. L. Zhou, Y. P. Zheng and J. Peng, *J. Solid State Chem.*, 2018, **258**, 786–791.
11 J. Q. Sha, P. P. Zhu, X. Y. Yang, N. Sheng, J. S. Li, L. J. Sun and H. Yan, *CrystEngComm*, 2016, **18**, 7049–7055.
12 B. W. Cong, Z. H. Su, Z. F. Zhao, B. Y. Yu, W. Q. Zhao, L. Xia, X. J. Ma and B. B. Zhou, *CrystEngComm*, 2017, **19**, 2739–2749.
13 Z. Z. He, D. Ma, B. R. Cao, X. Q. Li and Y. Lu, *Inorg. Chim. Acta*, 2018, **471**, 316–325.
14 X. L. Wang, R. Zhang, X. Wang, H. Y. Lin, G. C. Liu and H. X. Zhang, *Dalton Trans.*, 2017, **46**, 1965–1974.
15 C. J. Zhang, H. J. Pang, Q. Tang, H. Y. Wang and Y. G. Chen, *Dalton Trans.*, 2010, **39**, 7993–7999.
16 A. X. Tian, X. J. Liu, J. Ying, D. X. Zhu, X. L. Wang and J. Peng, *CrystEngComm*, 2011, **13**, 6680–6687.
17 H. Zhang, K. Yu, S. Gao, C. M. Wang, C. X. Wang, H. Y. Wang and B. B. Zhou, *CrystEngComm*, 2014, **16**, 8449–8456.
18 X. L. Wang, J. J. Cao, G. C. Liu, A. X. Tian, J. Luan, H. Y. Lin, J. W. Zhang and N. Li, *CrystEngComm*, 2014, **16**, 5732–5740.
19 K. T. Youm, H. K. Woo, J. Ko and M. J. Jun, *CrystEngComm*, 2007, **9**, 30–34.
20 J. R. Miecznikowski, J. P. Jasinski, M. A. Lynn, S. S. Jain, E. E. Butrick, A. E. R. Drozdoski, K. A. Archer and J. T. Panarra, *Inorg. Chim. Acta*, 2013, **394**, 310–321.
21 G. M. Seldrick, *SHELXS-97, Program for X-ray Crystal Structure Solution*, University of Göttingen, Göttingen, Germany, 1997.
22 G. M. Sheldrick, *Acta Crystallogr., Sect. C: Struct. Chem.*, 2015, **71**, 3–8.
23 G. M. Sheldrick, *SHELXL-97, Program for X-ray Crystal Structure Refinement*, University of Göttingen, Göttingen, Germany, 1997.
24 G. M. Sheldrick, *Acta Crystallogr., Sect. A: Found. Crystallogr.*, 2008, **64**, 112–122.
25 Y. B. Liu, W. J. Duan, X. B. Cui and J. Q. Xu, *Chem. Res. Chin. Univ.*, 2015, **31**, 4–8.
26 R. F. D. Luis, M. K. Urtiaga, J. L. Mesa, A. T. Aguayo, T. Rojo and M. I. Arriortuaa, *CrystEngComm*, 2010, **12**, 1880–1886.
27 Y. Q. Lan, S. L. Li, Z. M. Su, K. Z. Shao, J. F. Ma, X. L. Wang and E. B. Wang, *Chem. Commun.*, 2008, **1**, 58–60.
28 X. F. Kuang, X. Y. Wu, J. Zhang and C. Z. Lu, *Chem. Commun.*, 2011, **7**, 4150–4152.
29 H. Wu, J. Yang, Y. Y. Liu and J. F. Ma, *Cryst. Growth Des.*, 2012, **12**, 2272–2276.
30 L. Carlucci, G. Ciani and D. M. Proserpio, *Coord. Chem. Rev.*, 2003, **246**, 247–289.
31 L. Hou, J. P. Zhang and X. M. Chen, *Cryst. Growth Des.*, 2009, **9**, 2415–2419.
32 J. Q. Chen, Y. P. Cai, H. C. Fang, Z. Y. Zhou, X. L. Zhan, G. Zhao and Z. Zhang, *Cryst. Growth Des.*, 2009, **9**, 1605–1613.
33 Y. Huang, B. Yan and M. Shao, *J. Solid State Chem.*, 2009, **182**, 657–668.
34 Y. M. Li, C. Y. Xiao, X. D. Zhang, Y. Q. Xu, H. J. Luna and J. Y. Niu, *CrystEngComm*, 2013, **15**, 7756–7762.
35 H. J. Lun, X. F. Li, X. Wang, H. Y. Li, Y. M. Li and Y. Bai, *J. Mol. Struct.*, 2017, **1127**, 662–667.
36 Y. H. Zhang, W. Lei, Q. J. Wu, X. F. Xia and Q. L. Hao, *Microchim. Acta*, 2017, **184**, 3103–3111.
37 M. Musameh, M. R. Notivoli, M. Hickey, C. P. Huynh, S. C. Hawkins, J. M. Yousef and I. L. Kyratzis, *Electrochim. Acta*, 2013, **101**, 209–215.
38 H. J. Lun, S. S. Cui, H. J. Li, Q. Ping, H. H. Song, Y. M. Li, Y. Ru, Y. L. Bai and S. C. Xiang, *CrystEngComm*, 2015, **17**, 7029–7033.
39 H. J. Pang, J. Peng, J. Q. Sha, A. X. Tian, P. P. Zhang, Y. Chen and M. Zhu, *J. Mol. Struct.*, 2009, **922**, 88–92.
40 X. Wang, J. Peng, K. Alimaje, Z. Y. Zhang and Z. Y. Shi, *Inorg. Chem. Commun.*, 2013, **36**, 141–145.
41 X. L. Wang, Y. F. Bi, B. K. Chen, H. Y. Lin and G. C. Liu, *Inorg. Chem.*, 2008, **47**, 2442–2448.
42 Q. H. Guo, J. S. Huang, P. Q. Chen, Y. Liu, H. Q. Hou and T. Y. You, *Sens. Actuators, B*, 2012, **163**, 179–185.
43 S. Roy, V. Vemuri, S. Maiti, K. S. Manoj, U. Subbarao and S. C. Peter, *Inorg. Chem.*, 2018, **57**, 12078–12092.
44 Q. Y. Liu, W. F. Wang, Y. L. Wang, Z. M. Shan, M. S. Wang and J. K. Tang, *Inorg. Chem.*, 2012, **51**, 2381–2392.
45 Y. M. Li, X. F. Li, Y. Y. Wu, D. L. Collins-Wildman, S. M. Hu, Y. Liu, H. Y. Li, X. W. Zhao, L. Y. Jin and D. B. Dang, *Cryst. Growth Des.*, 2018, **18**, 7541–7547.
46 T. Fujii, K. Kodaira, O. Kawauchi and N. Tanaka, *J. Phys. Chem. B*, 1997, **101**, 10631–10637.
47 Y. M. Li, H. J. Lun, C. Y. Xiao, Y. Q. Xu, L. Wu, J. H. Yang, J. Y. Niu and S. C. Xiang, *Chem. Commun.*, 2014, **50**, 8558–8560.

